Dislocation Dynamics in Monocrystalline Si near the Melting Point Studied in Situ by X-Ray Bragg Diffraction Imaging

Serge William Neves Dias, Maike Becker, Hadjer Ouaddah, Isabelle Périchaud, Guillaume Reinhart, Nathalie Mangelinck-Noël, Gabrielle Regula

▶ **To cite this version:**

Serge William Neves Dias, Maike Becker, Hadjer Ouaddah, Isabelle Périchaud, Guillaume Reinhart, et al.. Dislocation Dynamics in Monocrystalline Si near the Melting Point Studied in Situ by X-Ray Bragg Diffraction Imaging. physica status solidi (b), 2022, 2100594, pp.1-8. 10.1002/pssb.202100594 . hal-03606956

HAL Id: hal-03606956
https://hal.science/hal-03606956

Submitted on 12 Mar 2022

HAL is a multi-disciplinary open access archive for the deposit and dissemination of scientific research documents, whether they are published or not. The documents may come from teaching and research institutions in France or abroad, or from public or private research centers.

L'archive ouverte pluridisciplinaire **HAL**, est destinée au dépôt et à la diffusion de documents scientifiques de niveau recherche, publiés ou non, émanant des établissements d'enseignement et de recherche français ou étrangers, des laboratoires publics ou privés.

Dislocation dynamics in monocrystalline Si near the melting point studied *in situ* by X-ray Bragg diffraction imaging

*Serge Neves Dias, Maike Becker, Hadjer Ouaddah, Isabelle Périchaud, Guillaume Reinhart, Nathalie Mangelinck-Noël, Gabrielle Regula**

This paper is dedicated to late Malcolm Heggie

Aix Marseille Univ, Université de Toulon, CNRS, IM2NP, Marseille, France

Email: gabrielle.regula@univ-amu.fr

Abstract

To study dislocation dynamics in a model sample, an intrinsic float zone (FZ) Si wafer is chosen as seed to initiate directional solidification. During the temperature ramp, a Von Laue diffraction spot is recorded by a camera. It provides time-resolved information on the evolution of silicon crystalline quality and on the defect nucleation locations and dynamics. With increasing temperature, dislocations are observed to propagate through the seed starting mainly from the sample edges. The effective thermomechanical local stress is estimated as low as $(1.2 \pm 0.4)\ 10^5$ Pa in a thermal gradient of $(1.8 \pm 0.2)\ 10^2$ K m^{-1}. The latter is sufficient to allow dislocation nucleation and motion at temperatures beyond (1523 ± 9) K. Dislocation velocity increases with temperature and reaches a maximum velocity of $(3.0 \pm 0.5)\ 10^{-4}$ m s^{-1} close to the silicon melting point. From the dislocation velocity measurements as a function of temperature, an activation energy of (3.1 ± 0.6) eV is estimated and this value is discussed, along with dynamical interactions between defects and dislocations.

Keywords: dislocation velocity, X-ray diffraction, silicon, PV-seeds, directional solidification, in situ, high temperature

1. Introduction

Nowadays, one of the bottlenecks to achieve good electrical efficiency of solar cells produced by directional solidification casting from Si seeds[1] are formation of dislocations and dislocation polygonization in the ingot and the seeds,[2, 3] as it results in the formation of highly electrically active sub-grain boundaries. In combination with an increased impurity contamination, the dislocation electrical activity becomes even worse, because precipitates can form in the dislocation core or in its vicinity.[4, 5] Dislocations

are of particular importance, especially when seeds are part of the Si ingot manufacturing process, like in the so-called cast-mono technique [6] or in the modified FZ method, [7] because dislocations can replicate from seeds into the up-grown crystal.[8] Moreover, the presence of dislocations during solidification can change the grain crystallographic facet growth mode, as modelled by Voronkov [9] and evaluated experimentally by Stamelou *et al.*.[10] Information on the silicon crystalline quality evolution of the ingots [11] and on the defect dynamics at temperatures close to the melting point are needed to get benchmark values for further modelling and simulation of dislocation behaviour.[12] To be able to predict the dislocation density, it is necessary to consider the total thermal history of the grown crystal. In addition, to develop defect engineering [13] and to achieve process optimization, main challenges are the determination of:

. the most active dislocation nucleation areas,

. the dislocation mobilities at high temperature,

. the dislocation interaction probability,

. the threshold critical resolved stress to nucleate and drive dislocations in motion, early in the heating of the seed up to the melting temperature.

Dislocation mobility in silicon has been extensively studied from a fundamental point of view in the last century, about 60 years after they had been postulated as crystalline defects and imagined by Volterra.[14, 15] Systematic studies of dislocations became possible as a result of the invention of the Dash process (necking), which allowed reducing the dislocation density below 10^2 cm^{-2} by pulling silicon float zone (FZ) or Czochralski (Cz) ingots.[16] Researchers were able to study the dynamics of designed populations of dislocations, intentionally introduced in samples containing dislocation densities lower than 10^2 cm^{-2} at controlled temperature (lower than 1573 K) and high stresses (always beyond 1 MPa).[17-20] Note that according to numerous studies on dislocations reported in the literature, it is assumed that dislocations obtained at temperature beyond about 773 K are dissociated into two Shockley partial dislocations, separated by a staking fault ribbon.[20] The main technique used to determine the velocity of these linear defects was based on the observation of the distance travelled by dislocations in a given amount of time (> 0.25 hours), which gives an average propagation

velocity. The dislocation position emergences were revealed *ex situ* after heating, either by etching or by X-ray diffraction topography.[21] Alexander and Haasen succeeded to model the Si experimental deformation behavior under uniaxial stress applied on the glide systems.[22] The model comprises several scalar equations which describe the macroscopic plastic deformation of a crystal by the so-called single-slip model including the formation and movement of dislocations. It neither takes into account cross-slip nor annihilation mechanisms. It is based on the relation between the rate of evolution of the plastic deformation $\dot{\varepsilon}$ and an average velocity v of N mobile dislocations with Burgers vector modulus $\boldsymbol{b}$:

$$\dot{\varepsilon} = N\,\boldsymbol{b}\,v \qquad (1).$$

The dislocation stochastic glide movement from one low atomic potential, called Peierls valley, to another one, is controlled by nucleation and motion of kinks along their line. It is a thermally activated process. The experimental dislocation mobility can be described by the following empirical law: [15]

$$v = v_0 \left(\frac{\sigma_r}{\sigma_0}\right)^m e^{\left(\frac{-Q}{kT}\right)} \qquad (2)$$

where v_0 and σ_0 are constants, m is the stress exponent, Q is the sum of the kink pair formation energy F_{kp} and the lateral migration energy of a kink W_m (secondary Peierls potential), k is the Boltzmann constant, σ_r is the effective resolved shear stress and T is the temperature. Q values depend on the dislocation character [17], on the impurity level of the Si matrix, [18, 20] on the applied stress σ [15] and possibly on the incident light.[23] Q is described by:

$$Q = F_{kp} - (\mu\,\sigma\boldsymbol{b}^3h^3/2\pi)^{1/2} + W_m \qquad (3)$$

where μ is the shear modulus of silicon and h is the distance between adjacent Peierls valleys ($h=\sqrt{3}\,\boldsymbol{b}/2$ in silicon).[15] The values reported in the literature for Q are ranging from 1.8 eV to 2.4 eV for temperatures lower than 1273 K and effective stresses between 1 to 500 MPa.[24] Q decreases under high applied stress, especially at low temperature range. Besides, a value of 4.0 eV is reported at 1573 K on phosphorus doped Si, indicating a change in the dislocation mobility mechanism when impurities are present, which is

assumed to be related to dislocation-point defect interactions although it is not yet fully understood.[19]

The resolved shear stress σ_r acting on a slip system results from the difference between the external applied stress on the dislocation and the background stress σ^* (provided it remains positive). In the Alexander-Haasen model, σ^* is proportional to the square root of the dislocation density N_D:[25]

$$\sigma^* = \mu b \sqrt{N_D} / [2\pi(1-\nu)] \qquad (4)$$

where ν is the Poisson ratio. Note that for N_D in the range of 10^4 cm^{-2} to 10^5 cm^{-2}, the corresponding values of σ^* at room temperature would be in the range of 0.1 to 0.3 MPa, according to Eq. (4).

The originality of the work presented here is that the dislocation characterisation is performed on live X-ray diffraction images recorded *in situ* during heating. Such experiments were performed at the European Synchrotron Radiation Facility (ESRF, beam line ID19). In the next section, the sample preparation, the measurement protocols of the resolved shear stress and the dislocation velocity are described. Then, the main results concerning defect interactions and dislocation mobility are presented and discussed.

2. Experimental details

2.1 Sample preparation and X-ray imaging setup

Intrinsic, double-face mirror-polished, float zone Si (110) Siltronix wafers are used as experimental material. The 400 µm thick wafers are cut to 38 × 7.7 mm^2 rectangular-shaped samples with a diamond wire saw. The crystallographic orientation of the sample is indicated in **Figure 1**. The three types of surfaces from the smallest to the largest surface area are denoted S1 to S3. The S2-type surfaces of the seed are mechanically polished to minimize the damage of the cutting process, finishing with a suspension of 3 µm large diamond particles. To reduce the number of surface dislocation sources (N_s) as much as possible, the whole sample is then chemically polished in CP4, which removes about 50-70 µm of material from all surfaces. The final thickness of the sample is between 260-300 µm over the sample length. It is inserted in a boron nitride (BN) crucible

assembly maintained by two molybdenum clamps, as shown in **Figure 1**. The crucible is then placed vertically along its largest dimension, inside the furnace constituted of two cylindrical heating resistors. The top heater is controlled at a higher temperature (temperature higher than the liquidus temperature of silicon) than the bottom heater (temperature lower than the melting temperature) to establish a vertical temperature gradient and ensure directional solidification. The furnace is operated under high vacuum conditions. A detailed description of the set up can be found in former papers.[26, 11] During heating, melting and further solidification, the Von Laue ($1\bar{1}1$) diffraction spot in transmission mode is indirectly recorded every 3 s by a CMOS camera.[26] The field of view (FOV) is 8.8 × 8.8 mm^2, with a pixel size of 4.3 μm^2. The mid-height of the sample is centred in the FOV. In figures 1, 3, 4 and 5, the vertical red arrow shows the direction of both thermal gradient and solid-liquid interface motion during the re-solidification phase, which allows determining the local thermal gradient in the sample (see section 2.2).

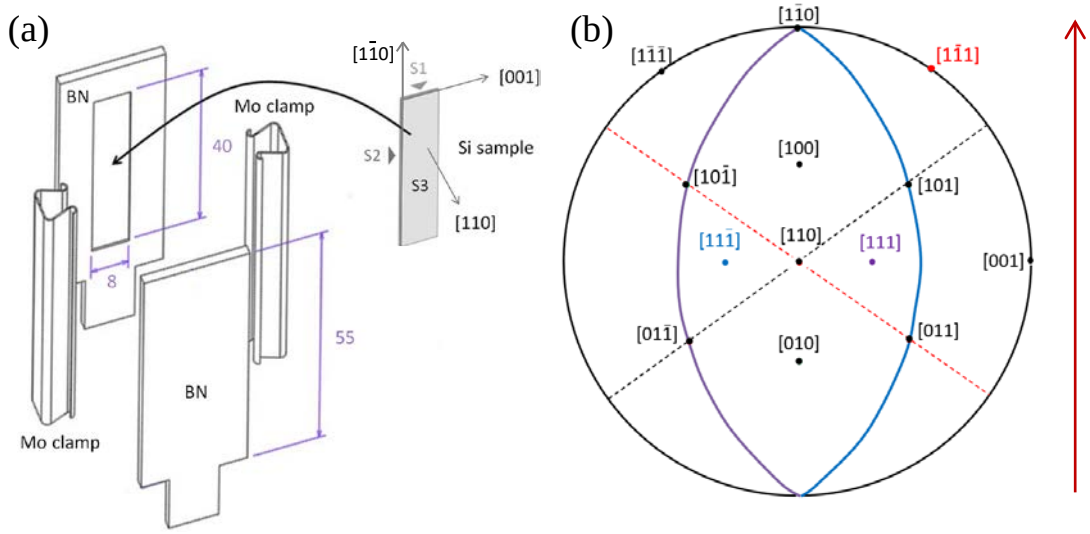

Figure 1 : Crucible and sample geometry; a) View of the elements of the crucible and the geometry of the silicon sample (dimensions are given in mm). The latter is placed in a 300 µm deep hollow, carved in a BN plate (see black curved arrow); b) stereographic projection of the sample crystal orientation with [110] as the centre pole, displaying the {111} traces and corresponding poles with matching colours, as well as the <110> sample edges.

The *in situ* experiments involve white X-ray incident beam and a high flux of X-ray photons, generating extra electron-hole pairs which, when non-radiatively recombining,

could lead to some photoplasticity.[23] Nonetheless, this effect is no longer effective at high temperature, since there is a large amount of available thermal or Auger recombination linked-phonons that are able to ease the formation of double kinks.

This work focuses solely on the last stage of the heating ramp of the sample (green area in **Figure 2**), to study the dislocation velocity close to the silicon melting temperature. The partial melting and solidification steps are also carried out, but are not reported in detail. They are mentionned because the solidification phase allows determining the local thermal gradient G_{local} (see section 2.2).[10, 27]

2.2 Imposed temperature and heating ramp

Silicon is heated according to a ramp (see **Figure 2**) applied on both resistive heaters. The temperature of the furnace is controlled within 1 K accuracy via the presence of two pyrometers located at the mid-height of each resistor of the furnace. The thermal gradient G between the two resistors can be tuned and is set to 4.0 10^3 K m^{-1} in the studied temperature range.

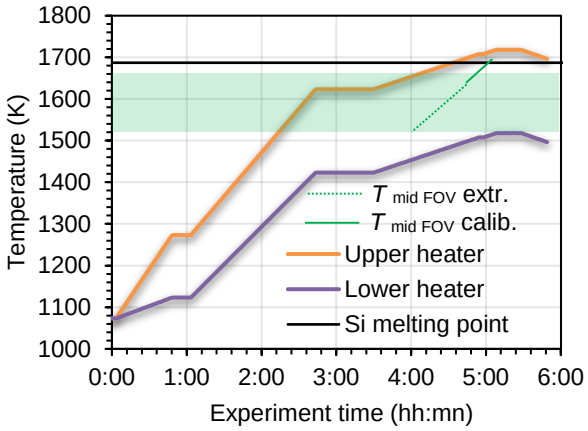

Figure 2: Temperature profiles of both heaters of the furnace and of the sample in the middle of the field of view (FOV, calibration and extrapolation). The black horizontal line corresponds to the Si melting isotherm. The temperature range whithin which the dislocation velocity measurements are carried out is highlighted with a green stripe.

The local thermal gradient G_{local} in the sample differs from the gradient G measured by the pyrometers, but can be determined by using the *in-situ* images of the melting and re-solidification process and by observing the dynamics of the solid-liquid interface.[10, 27] The analysis yields G_{local} of (1.8 ± 0.2) 10^2 K m^{-1}. G_{local} is the main driving force for the

dislocation motion in the studied temperature range. The deformation rate is varying as the temperature increases: it cannot be precisely quantified from equation (1), since the entire population of mobile dislocations cannot be visible in a single Laue spot. It is estimated in the 6 10^{-7} s^{-1}- 6 10^{-6} s^{-1} range which is very low compared to what is usually found in the literature.[28]

The temperature of the region of interest of the sample in the field of view is deduced by using the calibrated furnace temperature at mid-height of the field of view ($T_{\text{mid FOV}}$) and the local thermal gradient G_{local}, as follow:

$$T = T_{\text{mid FOV}} + G_{local} \times [\ (h_{FOV}/2)-((x_f - x_i)/2))] \qquad (5)$$

where h_{FOV} is the height of the field of view, and x_i and x_f are the dislocation tip positions at the beginning and the end of each measurement, respectively. The accuracy on the value of the local sample temperature in the region of interest is estimated to remain below 10 K. The time interval between two consecutive images is chosen to be able to measure dislocation speed up to 2.8 10^{-3} m s^{-1} and to limit the amount of stored data.

2.3 Ex-situ sample doping measurement

Since the crucible contains silicon dopant, and since dopants were reported to affect dislocation mobility at temperatures lower than 1073K,[18] a determination of the boron contamination from the crucible into the seed is performed after the experiment by resistivity measurements ρ, on un-melted and mechanically polished seed surfaces, using 4 aligned tips distant of 1.3 mm one from each other, using the following equation:

$$\rho = \frac{\pi}{\log(2)} w \frac{V}{I} \qquad (6)$$

where V is the applied voltage, I is the current and w is the local thickness of the sample (in cm). The latter is determined with a calliper and the boron level is given by the Irvin's curves.[29] The B concentration reaches (1.5 ± 0.5) 10^{17}at cm^{-3}.

2.4 Dislocation velocity and shear stress measurements

On as-recorded X-ray diffracted images, the dislocations appear in white due to the indirect recording system.[26] The recorded images are usually processed (by inversion and/or division) to increase the defect contrast. The vertical dark contrast along the S2-

type surfaces in **Figure 3** highlights the presence of strain due to residual cutting and polishing dammage.

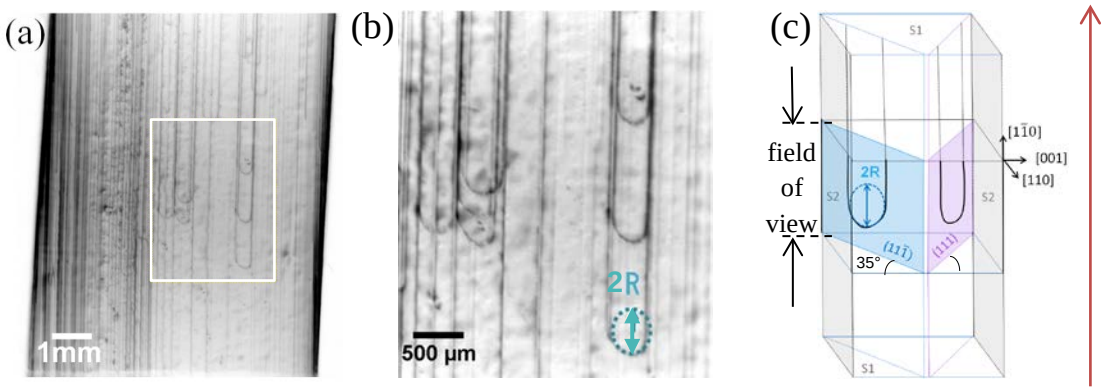

Figure 3: (a) FOV: recorded processed image of the $1\bar{1}1$ X-ray diffracted spot of the Si sample, at (1600 ± 9) K at mid-height of the field of view; (b) detailed view of the white rectangle in a) to highlight the radius of curvature of dislocation leading segments; c) sketch (not at scale, for sake of clarity) of the defects gliding on vertical {111} planes in the seed to illustrate the geometrical projection effect. The red vertical arrow shows the direction of the thermal gradient.

When the dislocations segments have entirely crossed the field of view they are visible as dark vertical straight dislocation segments in the X-ray diffraction images. When the dislocations expand towards the bulk, they are prevented to move out of the seed at its front and back S3-type surface by a surface reaction layer of Si_3N_4, which forms due to contact with the crucible. The distance between the two straight segments that belong to a dislocation loop is always similar and limited by the sample thickness and the thickness of the reaction layer. Hence, from the crystallographic orientation of the seed and the homogenous spacing, the thickness of the reaction layer can be estimated to reach about 20 µm.

Let us call x_f and x_i respectively the initial and final positions along the vertical axis of a dislocation tip in the field of view (see **Figure 4**), chosen for velocity measurements during a period of time t.

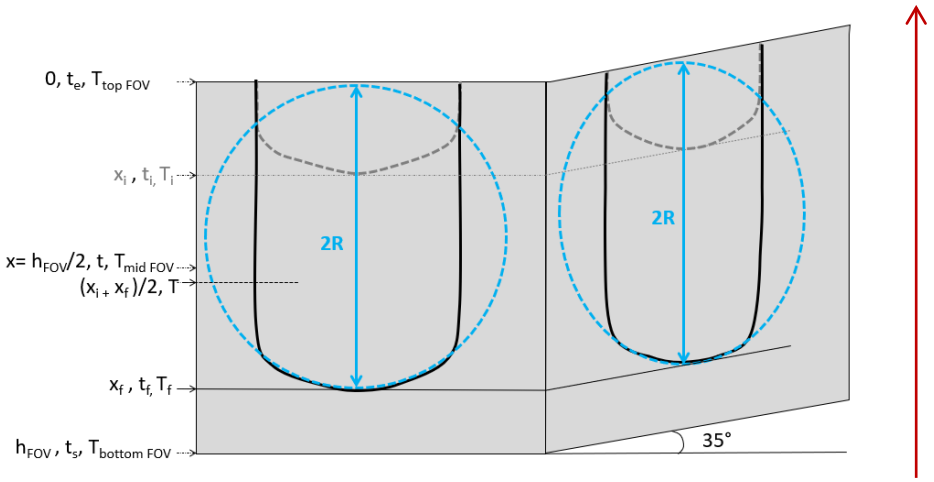

Figure 4: Sketch of dislocation leading segments during dislocation motion: left, the glide plane is observed along its normal; right, the glide plane is observed 35° away from its normal, following a horizontal plane. It corresponds to what is recorded by the CMOS camera. The grey dotted lines and black lines are respectively the initial and final positions of the dislocation segments, when measuring v. x, Δt and T are respectively the dislocation leading segment (tip) position, the duration of the tip crossing along the distance $X=(x_f-x_i)$, and the temperature at mid-crossed distance. The dislocation tip entrance time in the field of view t_e and its exit time t_s usually do not coincide with t_i and t_f which are respectively the initial and final times of the velocity measurement.

Since the glide planes are inclined vertically in projection, the distance $X=x_f-x_i$ crossed by the leading segment of a dislocation can be directly determined on the images. Then, the dislocation velocity v is simply calculated by dividing the distance X by the period of time Δt. Only dislocations which are crossing the entire field of view or are mobile over at least 5 mm are used to measure velocities.

The radius of curvature R of a mobile dislocation is measured on the images to calculate the effective resolved shear stress σ_r with the following equation:[30]

$$\sigma_r = \mu b/R \qquad (7).$$

The geometrical projection effect was taken into account when measuring the radius, since the glide planes parallel to the $[1\bar{1}0]$ seed length are 35° inclined as compared to the experimental configuration (see Figure 3c and Figure 4).

3. Results and discussion

3.1 Preferential dislocation nucleation areas and activated planes

The number of dislocation sources N_s and the seed surface preparation quality are found to be linked, which has been also observed in our previous work:[11] the poorer the

mechanical surface polishing quality, the larger N_s. Most of the sources are assumed to nucleate in S1-type surfaces, which are only chemically smoothed, and most of them are emitted from the upper hottest S1-type surface and move vertically in the $[\bar{1}10]$ direction towards the cooler S1 surface. This can be explained by the fact that the critical resolved shear stress to activate the sources decreases with increasing temperature.

Dislocation half loops expand along the entire length of the sample on {111} planes parallel to the temperature gradient (see vertical red arrow in **Figure 1** or **3**). In these glide planes, the resolved thermal-induced-stress is the highest, since these vertical glide planes are the first to be activated, as the sample temperature increases. When the seed starts to melt at its top, a change in the dynamics of the dislocation formation can be noticed: the number of emitted dislocations increases abruptly.

In fact, very few half loops of dislocations emitted from S2-type surfaces of the seed are observed crossing the field of view. Only a couple of dislocations nucleate in the field of view, the origin of which are either surface steps in the S3-type surfaces or bulk defects formed during the long stay of the seed at elevated temperature. In agreement with earlier work, we can assume that dislocations are mainly emitted from the edge sample surfaces (S1 and S2 ones).[11]

While the two glide family planes parallel to the thermal gradient are activated at relatively low temperature (873K), both edge-on glide planes (see their surface traces in dotted lines in **Figure 1** (b)) start containing dislocations at temperatures beyond 1650K. At this high temperature, some dislocation motion in the edge-on glide planes can be observed thanks to change of diffraction contrast along plane prints at the S3-type surface. It confirms that the glide planes parallel to the strongest temperature gradient are activated first, as observed in,[31] and that the dislocations gliding in these planes have the highest mobility. The activation of the edge-on glide plane at higher temperature than the vertical glide planes is mainly due to lower local resolved thermal induced-stress without excluding a possible lower N_s in the S2 surface-type. Note that the observed gliding dislocations in the edge-on glide planes can also come from the vertical glide planes by cross-slips, and that two thirds of dislocation types can be observed in the vertical inclined planes though only one third in the edge-on glide planes, as shown in **Figure 5** (e).

3.2 Observation of defect interactions

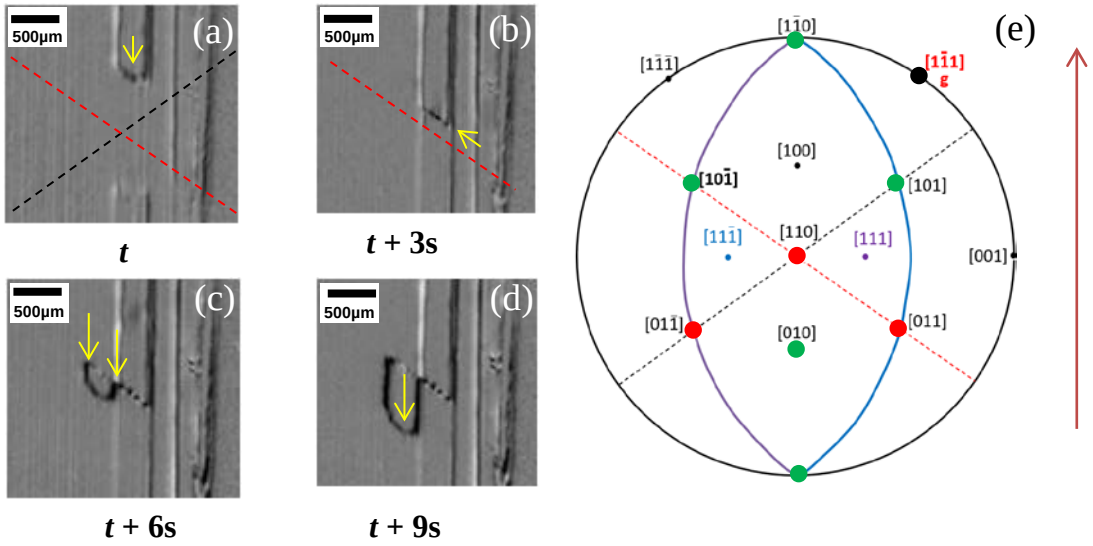

Figure 5: Successive X-ray diffraction images of the $1\bar{1}1$ X-ray diffracted spot of a dislocation double cross slip at (1650 ± 8) K (a) to (d) on $(11\bar{1})$ and $(1\bar{1}1)$ planes, the Burgers vector of which can be identified as $\boldsymbol{b} = \pm a/2[10\bar{1}]$ in (e). The either straight or paper-clip-shaped dislocations propagate in glide planes. The glide plane projections are drawn in purple and blue in (e); the dislocation motion direction is given by yellow arrows. The vertical thermal gradient is parallel to the $[1\bar{1}0]$ direction of the sample. In (a) traces of edge-on {111} glide planes are sketched by dotted black and red lines; (b) the tip of the dislocation cannot be observed since it is located in the edge-on glide plane (red family one, first cross slip); (c) second cross slip. (e) shows the Burgers vectors of these dislocations that cannot be observed in the recorded $(1\bar{1}1)$ Von Laue spot (red full circles), as well as the ones allowing dislocation observation (green full circles).

Studies of double cross-slip events allow determining the character of mobile dislocation leading segments. They are both 60° and screw type. Hence, velocity measurements given in the next section do not concern exclusively dislocation tips of 60° segments. **Figure 5 (**a)-(d) shows one of the two double cross slip sequences of the same dislocation for which we determined the Burgers vector $\boldsymbol{b} = \pm a/2[10\bar{1}]$. Note that the contrast of the images is increased by performing an image division by an average of its ten previous images to ease the observation of defect motion. During the heating ramp, eight cross-slips (four times each for two visible dislocations) are observed in the field of view at about 1650 K. It is in agreement with the high (5.5 eV) activation energy for cross slipping associated with a low occurrence probability (16% at 1234 K) reported in.[32] Nevertheless, it indicates that obstacles can form in the glide planes, although the seed is originally pure. Obstacle origin can be:

. Precipitates containing light impurities such as N, O or C due to the sample contact with the crucible. The induced lattice deformation of some of them, if too weak, cannot be observed by the X-ray diffraction imaging technique used here;

. Segregated impurities nearby dislocations due to the five hours stay at high temperature in the furnace;

. Sessile dislocation formation;

. Trailed vacancy complexes left by gliding dislocation segments.[33, 34]

The solid phase diffusion of boron from the crucible into the sample cannot affect the dislocation mobility through an electronic effect as proposed by Hirsch,[35] since the lower *Q* values in doped crystals in comparison with that of high-purity Si depend on the Fermi level position in the band gap. Indeed, it is supposed that a dislocation has a kink with an acceptor level and a donor level at ~0.5 and ~0.25 eV, respectively, above the valence band edge. At temperatures lower than 1073 K, point defects play the roles of accelerators of the dislocation motion, by means of preferential double kink formation on point defects, but also breaking of dislocation motion, as a result of generating obstacles for kink motion along the dislocation line.[36] At temperatures closer to the melting point, impurities become non-electrically effective to help kink formation, but they have a higher diffusivity, modifying W_m. B can thus only play a breaking role in the dislocation motion in this work, since Si reaches its intrinsic regime at about 1020 K.

A sole event of annihilation of leading dislocation segments coming from the hottest and coldest S1 surface-type is recorded and shown in **Figure 6**. They glide on a common plane or on adjacent planes (**Figure 6** (a) and (b)). As a result of the cancelling out after the junction, two notches are observed (**Figure 6**(c)).

Cross-slip events, annihilation, increase of dislocation nucleation when reaching the melting point can be seen lively in the supplementary material.

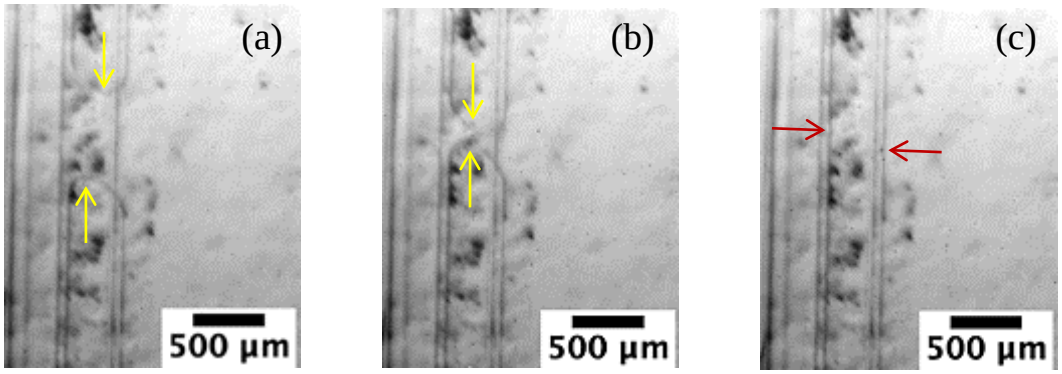

Figure 6: Annihilation of dislocations coming from both surface edges (S1) of the sample; t_a is a reference time for the display of the sequence. (a) and (b) at t_a and t_a + 3 s, two dislocations glide in opposite direction on a common plane or on adjacent planes (yellow arrows show the direction of motion of the leading segments); (c) at t_a + 6s: result of the cancelling out (junction leaving 2 notches shown by red arrows). The sample local temperature is (1580±9) K.

3.3 Dislocation velocity and activation energy

Slow down and even temporary back motion of dislocation leading segments due to the presence of neighbour dislocations (mobile or sessile) have been observed (available in the supplementary material). The thermomechanical stress, estimated at (0.12 ± 0.04) MPa according to Eq. (5) is mainly due to the presence of a thermal local gradient G_{local} = (1.8 ± 0.2) 10^3 K/cm. This stress is in the order of magnitude of the background stress σ* induced by a density of dislocations which is far from saturating the X-ray diffraction images. The observation limit is 10^6 cm^{-2} when the spatial resolution of the recording system is one micrometre. In other words, the average distance between dislocations is estimated to be ten times the spatial resolution of the recording system, due to the long-range strain field induced by dislocations. In this work, the spatial resolution being about 10 µm, the dislocation density is likely reaching few 10^4 cm^{-2}. Indeed, the thermomechanical stress remains greater than σ* induced by a dislocation density of 10^4 cm^{-2} (given by equation (4)), since the main vertical motion of dislocations remains along the seed length.

The maximum of the measured dislocation speed v is (0.3 ± 0.5) × 10^{-3} m/s at T = 1654 K. **Figure 7** shows the Arrhenius plot allowing the determination of the activation energy Q of the dislocations moving in the seed, the value of which is Q = (3.1 ± 0.6) eV.

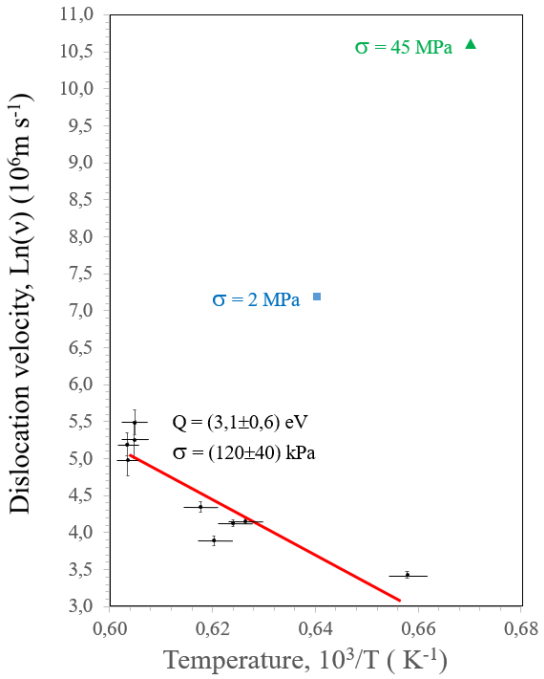

Figure 7: Arrhenius plot of dislocation velocity undergoing the same thermomechanical local stress, in a FZ Si seed in a temperature range close to the silicon melting point. Some literature values from references [19] and [20] are displayed in blue square and green triangle.

The dislocation velocities are averaged in the whole field of view. However, the stochastic motion behaviour has a greater effect on this kind of *in-situ* measurements (smaller sampling time) than on *ex-situ* ones. The studied temperature range is narrow, hence the data corresponding to the highest and lowest temperature have the most important weight in the determination of the *Q* value. Moreover, since the velocity measurements are carried out in a field submitted to a thermal gradient while the sample temperature increases, the accuracy of the temperature determination is weak, as can be seen with the error bars in **Figure 7**. As a prospect, the statistic should be improved with more experiments during heating experiments in isothermal conditions.

The activation energy value determined in our work is within the range of the values given in the literature for all investigated temperatures, doping and stress ranges in silicon. It is close but lower than the value (4.0 ± 0.1) eV found by Farber *et al.* who reported a dislocation velocity of (2.5 ± 7) × 10^{-3} m/s at 1573 K under a stress of 2 MPa.[19] However, a direct comparison is difficult due to the experimental conditions. On the one hand, their experiment was carried out at temperatures about 80 K lower than in this work, which is still close to the melting point. On the other hand, the applied stress in their experiments

was nearly 20 times greater than in this work, which should lead to a lower value of *Q* as shown in Eq. (3), provided that the kink formation is still stress-assisted even at high temperature. Assuming a stress exponent of m = 1 for silicon in Eq. (1), the dislocation velocities should be 7 times lower when the stress is lower by a factor of 20 (given by 20 × exp(-1654/1573)). Hence, the high temperature velocity measurements are in agreement with the ones from Farber *et al.*,[19] but the origin of the slight *Q* value discrepancy is not clear, since no stress level effect on *Q* value at elevated temperatures was ever reported.

The computed mobility of dissociated dislocations at low temperature (1000 K) is found to be strongly affected by the compatibility between the averaged stacking fault width between the partial dislocations and the period of the Peierls barrier.[37] Indeed, if the equilibrium distance between both partial dislocations (if Peierls barrier was not existing) is incommensurate with the real stacking fault width, the effect on the mobility increase is stronger for lowest stress ranges (about few MPa). From 2 to 20 MPa, there is a difference of nearly two orders of magnitude in the dislocation velocity values at 1000 K. Such difference does not exist when comparing the results of this work, performed at 0.1 MPa, with those reported by Farber *et al.*,[19] and carried out at 2 MPa. This would mean that the stacking faults have a width which is a multiple of the period of Peierls barrier (that is a multiple of a kink height) and that both partial dislocations have to move in unison, or that this effect is no longer effective at high temperature.

In this study, the measurements of individual dislocation velocities are not performed in a dislocation free material. The presence of neighbour dislocations can impede their motion due to mutual interactions, especially at low induced stresses in the kPa range, and as the number of dislocations increases in the sample. As long as the mean distance between to dislocations is more than 20 µm, a dislocation is assumed to be isolated. Nonetheless, let us remind that earlier work showed that the glide of a dislocation in a {111} plane would leave behind some debris which are found to be electrically active in comparison to a pristine {111} plane. They are assumed to be vacancy complexes being weak obstacles that cannot be observed by X-ray diffraction imaging.[34] Thus, the *Q* value should be considered as an effective one, due to all the actions taking place during the motion process such as reconstructions in the dislocation core atomic structure and

changes of the core state in jogs due to the high concentration of intrinsic point defects at such high temperature.

4 Conclusion

Preferential dislocation nucleation areas and dislocation interactions are observed during *in situ* observation of a Von Laue $1\bar{1}1$ diffraction spot corresponding to a seed heated up to the silicon melting temperature. Besides, individual dislocation velocities are measured. The low number of observed cross slips implies that dislocations are likely dissociated. The estimated thermomechanical local stress, $(120 \pm 40)\ 10^3$ Pa, induced by the $(1.8 \pm 0.2)\ 10^2$ K m^{-1} thermal gradient is of the same order of magnitude but remains greater than the background stress. This thermomechanical stress value is sufficient to allow dislocation nucleation and motion at temperatures beyond (1523 ± 9) K, since the Peierls stress becomes weaker at high temperature. The identification of the Burgers vector of those dislocations performing cross-slips shows that the leading dislocation segments are not all of 60° character. Their maximum dislocation velocity measured during the heating process is $(3.0 \pm 0.5)\ 10^{-4}$ m s^{-1} which is compatible with reported velocities.[19] An effective activation energy value Q = (3.1 ± 0.6) eV is derived. This value is within the interval of those found in previous studies at much lower temperature and higher stresses, [17, 18] and close but lower than (4.0 ± 0.1) eV reported in the (1323-1573) K temperature range at a stress of 2MPa.[19] The few tenths of eV discrepancy may be due to the fact that the measurements are carried out *in situ*, which results in short sampling times for each mobility measurement and enhances the stochastic dislocation motion behavior. Further set-up improvement is needed to better control both the chararacter of dislocation and the applied stress at high temperature. Furthermore, dislocation speed measurements in isothermal conditions will give more precise results. Some finite element calculations are in progress to determine the Von Mises stress in the seed in our experimental conditions, which will help in designing a new crucible. Moreover, the recording of at least two diffraction spots at the same time will provide additional information on the dislocation characteristics. Such improvements are foreseen in future developments.

Acknowledgements

The authors would like to thank the whole team of the ESRF ID19 beam line for their support, and the Deutsche Forschungsgemeinschaft (DFG) for Maike Becker's scholarship (project number 400343964).

References:

[1] M. G. Tsoutsouva, V. A. Oliveira, J. Baruchel, D. Camel, B. Marie, *Journal of Applied Crystallography* **2015**, *3*, 48.
[2] V.A. Oliveira, B. Marie, C. Cayron, M. Marinova, M.G. Tsoutsouva, H.C. Sio, T.A. Lafford, J. Baruchel, G. Audoit, A. Grenier, T.N. Tran Thi, D. Camel, *Acta Materiala* **2016**, *121*, 24-36.
[3] V.A. Oliveira, M. Rocha, A. Lantreibecq, M. G. Tsoutsouva, T. N. Tran-Thi, J. Baruchel, D. Camel, *Journal of Crystal Growth* **2018**, *489*, 42-50.
[4] M. Kittler, W. Seifert, K. Knobloch, *Microelectronic Engineering* **2003**, *66*, 281-288.
[5] S. Pizzini, A Gandolfi, S. Farina and M. Branciforti, *Materials Science and Engineering* **1990**, *B7*, 69- 82 69.
[6] A. Jouini, D. Ponthenier, H. Lignier, N. Enjalbert, B. Marie, B. Drevet, E. Pihan, C. Cayron, T. Lafford, D. Camel, *Prog. Photovolt. Res. Appl*. **2012**, *20*, 735-746.
[7] H.-J. Rost, R. Menzel, D. Siche, U. Juda, S. Kayser, F.M. Kießling, L. Sylla, T. Richter, *Journal of Crystal Growth* **2018**, *500*, 5–10.
[8] T. Ervik, G. Stokkan, T. Buonassisi, Ø. Mjøsd, O. Lohne, *Acta Materialia* **2014**, *67*, 99-2006.
[9] V. V. Voronkov, *Sov. Phys. Crystall.* **1973**, *17*.
[10] V. Stamelou, M. G. Tsoutsouva, T. Riberi-Beridot, G. Reinhart, G. Regula, J. Baruchel, N. Mangelinck-Noel, *Journal of Crystal Growth* **2017**, *479*, 1-8.
[11] M.G.Tsoutsouva, T. Riberi-Béridot, G. Regula, G. Reinhart, J. Baruchel, N. Mangelinck-Noël, *Phys. Status Solidi (a)* **2018**, *215*, 1700758.
[12] B. Gao, K. Jiptner, S. Nakano, H. Harada, Y. Miyamura, T. Sekiguchi, K. Kakimoto, *Journal of Crystal Growth* **2015**, *411*, 49-55.
[13] S. Woo, M. Bertoni, K. Choi, S. Nam, S. Castallenos, D. M. Powell, T. Buonassisi, H. Choi, *Solar Energy Materials and Solar Cells*, **2016**, *155*, 88-100.
[14] V. Volterra, *Annales scientifiques de l'Ecole Normale Supérieure* **1907**, *24*, 401-517.
[15] J.P. Hirth, J. Lothe, Theory of Dislocations, Wiley, New York **1982**.
[16] W.C. Dash, *J. Appl. Phys*. **1959**, *30*, 459.
[17] A. George, C. Escaravage, G. Champier, W. Schroter, *Phys. Status Solidi (b)* **1972**, *483*, 53.
[18] A. George and G. Champier, *Phys. Status Solidi (a)* **1979**, *53*, 529.
[19] Y. Farber, V. I. Nikitendo, *Phys. Status Solidi (a)* **1982**, *73*, K141.
[20] I. Yonenaga, *Semicond. Sci. Technol.* **2020**, *35*, 043001.

[21] A. R. Lang, *J. Phys. D: Appl. Phys.* **1993**, *26*, A1.
[22] H. Alexander, P. Haasen, *Solid State Phys.* **1968**, *22*, 27.
[23] K.H. Küsters and H. Alexander, *Physica* **1982**, *116B*, 594-599.
[24] I. Yonenaga, *Engineering Fracture Mechanics* **2015**, *147*, 468-479.
[25] N. Banos, J. Friedrich, G. Müller, *Journal of Crystal Growth* **2008**, 310, 501–507.
[26] M. Becker, G. Regula, G. Reinhart, E. Boller, J. P. Valade, A. Rack, P. Tafforeau, N. Mangelinck-Noël, *Journal of Applied Crystallography* **2019**, *6*, 52.
[27] Thècle Riberi-Beridot, Maria Tsoutsouva, Gabrielle Regula, Guillaume Reinhart, I. Périchaud, José Baruchel, N. Mangelinck-Noël, *Journal of Crystal Growth* **2017**, *466* 64-70.
[28] I. Yonenaga and K. Sumino, *Phys. Status Solidi (a)* **1978,** 50, 685.
[29] J. C. Irvin, Bell System Technical Journal **1961**, *41 (2)* 387-410.
[30] H. Gottschalk, *J. Phys. Colloq.* **1983**, 44, C4–69.
[31] A.N. Danilewsky, J. Wittge, A. Croell, D. Allen, P. McNally, P. Vagovič, T. dos Santos Rolo, Z. Li, T. Baumbach, E. Gorostegui-Colinas, J. Garagorri, M.R. Elizalde, M.C. Fossati, D.K. Bowen, B.K. Tanner, *Journal of Crystal Growth* **2011**, *318*, 1157-1163.
[32] H.J. Möller, H. Ewalt and P. Haasen, *Phys. Status Solidi (a)* **1979**, *55*, 469.
[33] V. G. Eremenko and E. B. Yakimov, *The European physical journal applied physics* **2004**, *27*, 349-351.
[34] M. A. Khorosheva, V. V. Kveder, and M. Seibt, *Phys. Status Solidi (a)* **2015**, *212* (8), 1695-1703.
[35] Hirsch P B, *J. Phys. Colloq.* **1979**, *40 C6*, 117-21.
[36] Y. Farber, Y. L. Iunin, and V. I. Nikitendo, *Phys. Status Solidi (a)* **1986**, *97*, 469.
[37] W. Cai, V.V. Bulatov, J. F. Justo, A. S. Argon, S. Yip, *Physical Review Letters* **2000**, *84*, (15) 3346- 3349.